

A Stochastic Model for Automatic Extraction of 3D Neuronal Morphology

Sreetama Basu¹, Maria Kulikova², Elena Zhizhina³,
Wei Tsang Ooi¹, and Daniel Racoceanu^{2,4}

¹ National University of Singapore, Singapore

² University Pierre and Marie Curie, Paris, France

³ Institute of Information Transmission Problems, Russia

⁴ CNRS, France

Abstract. Tubular structures are frequently encountered in bio-medical images. The center-lines of these tubules provide an accurate representation of the topology of the structures. We introduce a stochastic Marked Point Process framework for fully automatic extraction of tubular structures requiring no user interaction or seed points for initialization. Our Marked Point Process model enables unsupervised network extraction by fitting a configuration of objects with globally optimal associated energy to the centreline of the arbors. For this purpose we propose special configurations of marked objects and an energy function well adapted for detection of 3D tubular branches. The optimization of the energy function is achieved by a stochastic, discrete-time multiple birth and death dynamics. Our method finds the centreline, local width and orientation of neuronal arbors and identifies critical nodes like bifurcations and terminals. The proposed model is tested on 3D light microscopy images from the DIADEM data set with promising results.

1 Introduction

Advances in imaging technologies generate huge volume of microscopy data. Manual analysis of such data is prohibitively expensive in terms of the expert man-hours required. At present, high resolution, high content 3D data is becoming more and more prevalent. Thus, a fully automatic, stochastic rather than deterministic data exploration strategy, combining both local and global image evidence, is desired [1].

Neurite tracing methods connect paths of maximum neuriteness voxels locally between sets of seed points to extract the global neurite structure. A common drawback of existing methods is their dependence on seed points [2]. Often, manual intervention is required to select the optimal seed points. Unavailability of seed points can even lead to entire branches going undetected. Not only for neurons, seed points are a relevant concern for all kinds of tubular structure extraction scenarios [3]. Commonly, multiscale Eigen-analysis [4], in combination with gradient information [5] or intensity ridge traversal [6] are used to detect seeds on tubule centrelines. These filters find voxels maximizing a vesselness measure by collecting responses over a range of filter scales. They are computationally intensive as multiple scales and orientations of the filters are convolved with the image data at every voxel. With increasing volume of data and considering 3D orientations of neurites, deterministic filter response maximization



Fig. 1. (a) Minimum intensity projection of intensity inverted (for ease of visualisation) Olfactory Projection Fibers (OPF) data obtained by confocal microscopy. (b) The extracted network with the proposed model visualised on a projection of the OPF data. We restrict overlap of object to have a sparse density on the branches and yet get a sense of the continuity of the neurites.

is an infeasible option, considering the huge solution space that is required to be explored. The results will be sensitive to initialization, necessitating human intervention. Machine learning techniques like SVMs for automatic seed selection have been proposed in the literature [7]. But their dependence on availability and quality of learning data, however, make them an unattractive choice.

We develop an efficient Marked Point Process (MPP) framework for extraction of neuronal structures from 3D data without greatly increasing the computational complexity of sampling and estimation, in contrast to existing MPP based 2D methods [8],[9]. Firstly, spheres are chosen as MPP objects, in particular because it gives one dimensional object space but allows to simultaneously extract center line, size and local orientation of branches. Secondly, to find the Maximum A Posteriori (MAP) estimate of the optimal configuration, we sample from the object configuration space using a Multiple Birth and Death (MBAD) dynamics embedded in a Simulated Annealing scheme [10]. The MBAD dynamics reduces computational cost over traditional Reversible Jump Monte Carlo Markov Chain samplers by avoiding proposal kernel computations and leads to faster convergence.

2 3D Marked Point Process Model

The *Point Process* models were first introduced in [11] to exploit random fields whose realizations are configurations of random points describing a spatial distribution of data.

2.1 From Point to Parametric Marked Point Process

We consider a point process \mathcal{X} existing in $K = [0, X_{max}] \times [0, Y_{max}] \times [0, Z_{max}]$, where K is a bounded, connected subset of \mathbb{V}^3 , the image domain. In the Marked Point Processes, each point x_i is associated with additional parameters (marks) m_i to define an object $\omega_i = (x_i, m_i)$. Here, $x_i \in K$ and $m_i \in M$ and the Marked Point Process \mathcal{Y} is defined on $K \times M$. The *configuration space* of the objects is given by $\Omega = \cup_{n=0}^{\infty} \Omega_n$.

where Ω_0 is the empty set, each $\Omega_n, n \in \mathbb{N}$ is the set of unordered sets (configurations) containing n objects and $\gamma_n \in \Omega_n, \gamma_n = \{\omega_1, \dots, \omega_n\}$. Note that n can be arbitrary, and in the following sections of the paper the elements of configuration $\gamma \in \Omega$ (with an arbitrary number of elements) will be denoted as ω_i , where $i = 1 \dots n$.

2.2 Gibbs's Distribution and Energy of Configuration

The Marked Point Processes are defined by their probability density w.r.t. the reference Poisson process. Given a real, bounded below function $U(\gamma)$ in Ω , the Gibbs distribution μ_β in terms of the density $p(\gamma) = \frac{d\mu_\beta}{d\lambda}(\gamma)$ w.r.t. Lebesgue-Poisson measure λ on Ω is defined as:

$$p(\gamma) = \frac{z^{|\gamma|}}{Z_\beta} \exp[-\beta U(\gamma)]. \quad (1)$$

Here, parameters $z, \beta > 0$ and Z_β is a normalizing factor. In the Gibbs energy model, the optimum object configuration $\hat{\gamma}$ corresponds to the minimum global energy, where γ represents the configuration of objects:

$$\hat{\gamma} = \arg \max_{\gamma} p(\gamma) = \arg \min_{\gamma} U(\gamma). \quad (2)$$

$$U(\gamma) = \sum_{\omega_i \in \gamma} U_d(\omega_i) + \sum_{\substack{\omega_i, \omega_j \in \gamma; \\ \omega_i \sim \omega_j}} U_i(\omega_i, \omega_j) + \sum_{\omega_i \in \gamma} U_c(\omega_i), \quad (3)$$

where the operation \sim is defined as a neighborhood relation: $\omega_i \sim \omega_j = |\omega_i, \omega_j \in \gamma : |x_i - x_j| < tD|$ and D is distance between centres of objects ω_i and ω_j , and $t \in \mathbb{N}$. U_d represents the data energy, U_i is the interaction prior energy and U_c is the connection prior energy. We seek to minimize the global energy $U(\gamma)$. To find the minimizer $\hat{\gamma}$ means to find the number n of objects in the required configuration and to find positions of all n objects in the configuration $\hat{\gamma}$.

3 Energy Modeling for 3D Neuronal Network Extraction

Our aim is to extract the neuronal branches by generating a configuration of objects fitted to the points of maximum medialness measure on the image volume. For this purpose, we adopt spheres as objects $\omega_i = (x_i, r_i)$, $x_i \in \mathbb{V}^3$, $r_i \in [r_{min}, r_{max}]$ and $\omega_i(x_i, r_i) = (y_i : |x_i - y_i| \leq r_i)$ where y_i are voxels in the image domain \mathbb{V}^3 . The stochastic optimization and random sampling strategy of the object configuration space, which also defines our filter space, extracts an optimal configuration of objects whose radii correspond to the scales of the filters maximizing the responses at their centre voxels in the image data. In the following section we describe each of the energy components in detail.

3.1 Data Energy

Our data energy response is based on the tubularity filter proposed in [12] and the interested reader may refer it for complete details. The Hessian is a second order partial derivative of image data containing local structural information. Its principal components determine the tangent direction and normal plane of the local neurite structures.

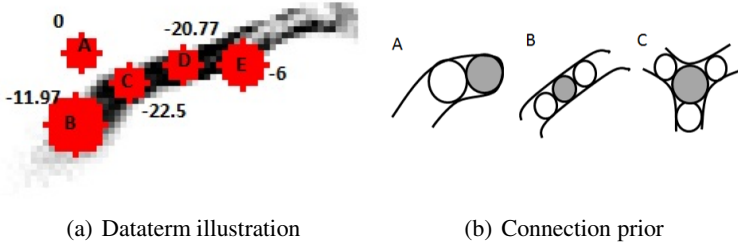


Fig. 2. (a) High negative energies indicate “good” objects (eg. objects B,C,D) i.e. objects situated on the branch centreline and the same size as the local branch width. “Bad” objects, for example, on the background (object A) or not centred correctly on the branch (object E) have low probabilities of survival in the configuration during the energy minimization scheme. (b) Each sub configuration is identified by its characteristic connection energy - evaluated w.r.t. the number of neighbors with direct data connection with the current object (shaded in the image). A: Terminal. B: Anchor points along the length of a branch. C: Bifurcation junction.

The scale of the Hessian σ_H is uniformly sampled from the radius range $[r_{min}, r_{max}]$. The medialness measure $M(\omega_i)$ is obtained by taking an integral of the image gradient at scale σ_G along the circumference of the cut of the spherical object on the normal plane defined by V_1 and V_2 -

$$M(\omega_i) = \left| \frac{\pi}{2} \int_{\theta=0}^{2\pi} \nabla I^{(\sigma_G)}(x_i + r_i V_\theta) d\theta \right|. \tag{4}$$

Here, $V_\theta = \cos(\theta)V_1 + \sin(\theta)V_2$ is a rotating phasor in the normal plane sampling gradient information at radial distance r from the center $x_i = [x, y, z]^T, x_i \in \mathbb{V}^3$ of the object. The medialness measure varies greatly for thin or weakly contrasted neurite branches, a common occurrence in case of microscopy images due to injection of noise and non-homogeneous staining of the neurons. Thus, a user defined optimal global threshold to reject structured noise and background artifacts is difficult to obtain. So, to discriminate between “good” and “bad” objects an adaptive thresholding of the medialness response is performed based on the gradient response at the tube’s center $M_c(\omega_i) = |\nabla I^{(\sigma_H)}(x_i)|$. The data energy term is then defined as follows:

$$U_d(\omega_i) = \begin{cases} -(M(\omega_i) - M_c(\omega_i)), & \text{if } M(\omega_i) > M_c(\omega_i) \\ 0, & \text{otherwise.} \end{cases} \tag{5}$$

3.2 Pair-Wise Interaction Prior Energy

This term is a pair-wise interaction potential for objects in each other’s zone of influence. It avoids crowding together of spheres along the neuronal processes and favors continuity of network by merging of close lying disconnected fragments, a common occurrence in microscopy data due to inhomogeneity in branch intensity and poor contrast with background. Around every object exists an immediate zone of repulsion followed by a concentric zone of attraction. Two energy potentials are defined: U_+ is repulsive

in nature to penalize objects lying too close to each other, and U_- is attractive in nature to favor objects in reasonable distances of each other.

$$U_i(\omega_i, \omega_j) = \begin{cases} U_+, & \text{if } d < d_r \\ U_-, & \text{if } d_r \leq d \leq d_a \\ 0, & \text{if } d > d_a. \end{cases} \quad (6)$$

Here, d is the Euclidean distance between the centres of the spheres; d_r and d_a ($d_r < d_a$) are respectively the repulsive and attractive distances, d_r, d_a are multiples of $r_i + r_j$. By varying d_r and d_a , density of spheres along the neuronal branches can be controlled.

3.3 Connection Prior Energy

The second prior is a multi-object interaction potential, incorporating constraints on the connection among objects. Depending on the number of objects $k(\omega_i) = |\omega_j \in \gamma : d_r < d(\omega_i, \omega_j) < d_a|$, in the neighborhood, the prior term can also be used to determine branching points and termination points along neuronal processes, see Fig. 2(b).

$$U_c(\omega_i) = \begin{cases} E_1, & \text{if } k(\omega_i) = 0 \\ -E_1, & \text{if } k(\omega_i) = 1 \\ -E_2, & \text{if } k(\omega_i) = 2, 3 \\ -E_2, & \text{if } k(\omega_i) = 4 \\ E_1, & \text{if } k(\omega_i) > 4. \end{cases} \quad (7)$$

This association of favorable energy potentials E_1 and E_2 with particular local sub-configurations encourage accurate detection of critical nodes. At the same time, it discourages isolated objects in the configuration, which are likely to correspond to cell nuclei or other such background structures.

3.4 Optimization

The complexity of optimization of the global energy depends directly on the size of the sampling space of the objects, which we limit by the adoption of spherical objects, with a 1-dimensional parameter space. The optimum global energy is defined over the space of union of all possible configurations, considering an unknown a-priori number of objects. To obtain the optimal configuration of the objects on the image data, we use MAP estimation (Eq.2). We sample from the probability distribution μ_β using a Markov chain of the discrete-time Multiple Birth and Death dynamics defined on Ω and apply a Simulated Annealing scheme. At every iteration, a transition is considered from current configuration γ to $\gamma' \cup \gamma''$ where $\gamma' \subset \gamma$ and γ'' is any new configuration. The corresponding transition probability is given by:

$$P(\gamma \rightarrow \gamma' \cup \gamma'') \sim (z\delta)^{|\gamma''|} \prod_{\omega_i \in \gamma \setminus \gamma'} \frac{\alpha_\beta(\omega_i, \gamma)\delta}{1 + \alpha_\beta(\omega_i, \gamma)\delta} \prod_{\omega_i \in \gamma'} \frac{1}{1 + \alpha_\beta(\omega_i, \gamma)\delta}, \quad (8)$$

where $\alpha_\beta(\omega_i, \gamma) = \exp(-\beta(U(\gamma \setminus \omega_i) - U(\gamma)))$. The convergence properties of the Markov Chain to the global minimum under a decreasing scheme of parameters δ and $\frac{1}{\beta}$ are proved in [10]. The probability of death of an object depends on both the

Algorithm 1. Multiple Birth and Death

Initialize

Discrete time-step $\delta = \delta_0$ and inverse temperature $\beta = \beta_0$.

Now, alternate between birth and death step until stop condition is met:

Birth

(a) Generate a configuration of spheres $\gamma \in \Omega$, from the Lebesgue-Poisson distribution with intensity $z = \delta z_0$ for centers, with independent radii uniformly distributed on $[r_{min}, r_{max}]$. A hard core repulsion δ_ϵ is added with ϵ equal to one pixel.

(b) $\gamma' \cup \gamma''$: Add the new set of objects γ'' to the “surviving” ones $\gamma' \subset \gamma$ to get the current configuration γ .

Death

(a) Sort the objects of the current configuration according to their data energy $U_d(\omega_i)$, for the purpose of accelerating computation;

(b) Each object ω_i in the configuration γ , is removed with probability $p(\omega_i, \gamma) = \frac{\delta \alpha_\beta(\omega_i, \gamma)}{1 + \delta \alpha_\beta(\omega_i, \gamma)}$;

Termination

Terminate if all and only objects added in the birth step of current iteration are removed. Else, update γ , decrease $\delta, \frac{1}{\beta}$ according to a geometric annealing schedule and go to the birth step.

temperature and its relative energy in the sub-configuration; whereas, birth of object is independent of both energy and temperature and is spatially homogenous. In this way, the iterative process finds a configuration $\hat{\gamma}$ minimizing the global energy Eq. 3.

4 Experiments and Results

We test the performance of our proposed model on 3D light microscopy image stacks from the DIADEM Challenge database [13]. See Fig.3 and Fig.1. Although our method is not sensitive to the initialization of the configuration, to speed up convergence to the optimum configuration, the birth of the objects are restricted to a region of interest defined by the dilation of the maximum intensity projection of the original data stack for OPF and NL1 datasets. On the CCF data, obtained by Brightfield Microscopy, the configuration space is limited to a layered depth map obtained by a maximum intensity projection of the data. Our unoptimized Matlab implementation takes 57 mins, 3 hrs 29 mins, 1hr 33 mins to converge on NL1, OPF and CCF respectively, on a PC running Intel Core i7 processor, 3.4 GHz with 8GB RAM.

The *parameters of the priors* are set to $-U_+ = 10$, $U_- = -2$, $E_1 = 1.5$ and $E_2 = 2.0$, as described in the literature [14]. The *sampling parameters* are learnt from experiments and set as $\beta_0 = 1$ and δ_0 to approximately three to five times the number of objects expected in the final configuration. The objects are sampled uniformly from the radius ranges $[1, 10]$, $[1, 3]$ and $[1, 25]$ for OPF, NL1 and CCF datasets respectively. The deviation of the extracted points set (P) using our proposed model from gold standard manually delineated centrelines (G) is compared in Table 1 in the following way:

$$\max(P, G) = \max\left(\min_{p \in P, g \in G} (f(p, g))\right) \quad (9)$$

$$\text{avg}(P, G) = \text{avg}\left(\min_{p \in P, g \in G} (f(p, g))\right) \quad (10)$$

$$\text{err}_r(P, G) = \text{avg}(|r_p - r_g|: \min_{p \in P, g \in G} (f(p, g))) \quad (11)$$

where $f(p, g)$ represents Euclidean distance of the concerned points and r_p and r_g are radius at point p and g respectively. Thus, our method produces an automatic and reliable extraction of neuronal morphology. It is robust to small branch discontinuities, intensity variations due to inhomogeneous labeling, noise and background interference.

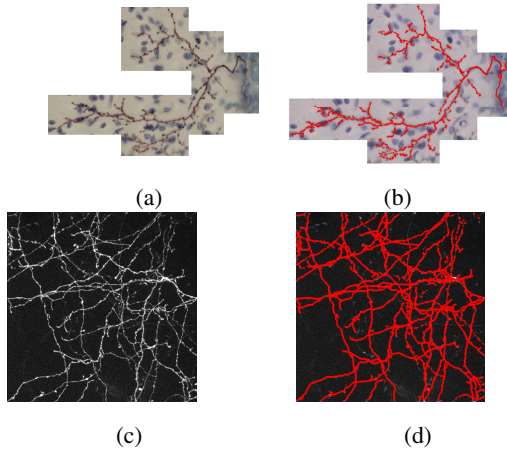


Fig. 3. (a) Minimum intensity projection of Cerebellar Climbing Fibers (CCF) obtained by Transmitted Light Brightfield microscopy. (b) The neuronal network extraction with the proposed model visualised on a slice CCF data. (c) Maximum intensity projection of Neocortical Layer 1 Axons (NL1) obtained by 2-photon Laser Scanning microscopy. (d) The neuronal network extraction with the proposed model on the projection of the NL1 data. These results are obtained with a high density of objects, allowing overlap to fully reconstruct the fuzzy and blurred segments of the neurites.

Table 1. Evaluation of our proposed method against Gold Standard manual extraction. The units of reporting error are anisotropic image voxels. The errors are higher along the z-axis due to the differential resolution of original data. *: ground truth radius not available.

| Dataset | Resolution | Centreline deviation | | | Radius |
|---------|--------------|----------------------|-------------|----------------------------|---------------|
| | | $avg(P, G)$ | $max(P, G)$ | Points under 1 voxel error | $err_r(P, G)$ |
| OP1 | 512x512x60 | 1.231 | 3.9 | 80.14% | 0.5243 |
| OP2 | 512x512x88 | 1.065 | 2.5319 | 78.72% | * |
| OP4 | 512x512x67 | 1.4064 | 2.7154 | 83.71% | 0.5786 |
| CCF1 | 6120x4343x34 | 2.67 | 6.5869 | 66.23% | 1.7656 |
| NC01 | 512x512x60 | 1.1398 | 2.0119 | 79.12% | * |

5 Conclusion

To conclude, we present a MPP model for unsupervised network extraction that is fully automatic and requires neither seed points nor manual intervention. The proposed method significantly improves network detection by reconstructing blurred and fuzzy segments of networks due to connectivity priors of the energy function. Our work can also be viewed as a stochastic optimization of scale-orientation space for matched

filters, developing a connected network of maximum vesselness points on tubular structures. The stochastic optimization to the global minimum and the random nature of data exploration makes it preferable for large, high content microscopy data-sets. The obtained results demonstrate its reliability and robustness for fully automated analysis of neuronal morphology.

So far, we only extract the neuronal structures by a configuration of uniformly spaced MPP objects. A future extension of our work might be neuronal reconstruction, where the extracted centreline, local width and orientation information along with detected critical nodes will aid in a connected, tree hierarchical representation of the neuronal arbors. Additionally, studies of the sensitivity and robustness of our model w.r.t. the model parameters and automatic estimation of the critical parameters are important, as that would increase the applicability of the family of Marked Point Process based methods.

References

1. Meijering, E.: Neuron tracing in perspective. *Cytometry Part A* 77(7), 693–704 (2010)
2. Türetken, E., Blum, C., González, G., Fua, P.: Reconstructing geometrically consistent tree structures from noisy images. In: Jiang, T., Navab, N., Pluim, J.P.W., Viergever, M.A. (eds.) MICCAI 2010, Part I. LNCS, vol. 6361, pp. 291–299. Springer, Heidelberg (2010)
3. Kirbas, C., Quek, F.: A review of vessel extraction techniques and algorithms. *ACM Computing Surveys* 36(2), 81–121 (2004)
4. Frangi, A.F., Niessen, W.J., Vincken, K.L., Viergever, M.A.: Multiscale vessel enhancement filtering. In: Wells, W.M., Colchester, A.C.F., Delp, S.L. (eds.) MICCAI 1998. LNCS, vol. 1496, pp. 130–137. Springer, Heidelberg (1998)
5. Krissian, K., Malandain, G., Ayache, N., Vaillant, R., Troussset, Y.: Model-based multiscale detection of 3d vessels. In: *CVPR*, pp. 722–727 (1998)
6. Aylward, S.R., Bullitt, E.: Initialization, noise, singularities and scale in height ridge traversal for tubular object centerline extraction. *IEEE Trans. Med. Imaging* 21(2), 61–75 (2002)
7. González, G., Fleuret, F., Fua, P.: Learning rotational features for filament detection. In: *CVPR*, pp. 1582–1589 (2009)
8. Lacoste, C., Finet, G., Magnin, I.E.: Coronary tree extraction from x-ray angiograms using marked point processes. In: *ISBI*, pp. 157–160 (2006)
9. Sun, K., Sang, N., Zhang, T.: Marked point process for vascular tree extraction on angiogram. In: Yuille, A.L., Zhu, S.-C., Cremers, D., Wang, Y. (eds.) *EMMCVPR 2007*. LNCS, vol. 4679, pp. 467–478. Springer, Heidelberg (2007)
10. Descombes, X., Minlos, R., Zhizhina, E.: Object extraction using a stochastic birth-and-death dynamics in continuum. *Journal of Math. Imaging and Vision* 33(3), 347–359 (2009)
11. Baddeley, A., Van Lieshout, M.: Stochastic geometry models in high-level vision. *Journal of Applied Statistics* 20(5-6), 231–256 (1993)
12. Pock, T., Janko, C., Beichel, R., Bischof, H.: Multiscale medialness for robust segmentation of 3d tubular structures. In: *Proceedings of the Computer Vision Winter Workshop*, pp. 93–102 (2005)
13. Brown, K., Barrionuevo, G., Canty, A., De Paola, V., Hirsch, J., Jefferis, G., Lu, J., Snippe, M., Sugihara, I., Ascoli, G.: The diadem data sets: Representative light microscopy images of neuronal morphology to advance automation of digital reconstructions. *Neuroinformatics*, 1–15 (2011)
14. Cariou, P., Descombes, X., Zhizhina, E.: A point process for fully automatic road network detection in satellite and aerial images. *Problems of Information Transmission* 10(3), 247–256 (2010)